# Frustration-mediated crossover from long-range to short-range magnetic ordering in $Y_{1-x}Lu_xBaCo_4O_7$

Sevda Sahinbay,[1,2,3,*] Hong Zheng,[2] J. F. Mitchell,[2] Stephan Rosenkranz ![ORCID],[2] and Omar Chmaissem ![ORCID][2,3]

[1]*Department of Engineering Physics, Istanbul Medeniyet University, Istanbul 34700, Turkey*
[2]*Materials Science Division, Argonne National Laboratory, Lemont, Illinois 60439, USA*
[3]*Department of Physics, Northern Illinois University, DeKalb, Illinois 60115, USA*

The $R$BaCo₄O₇ system is a prototype geometrically frustrated magnet in which kagome planes and triangular layers of Co-O tetrahedra interleave. For $R$ = Y, an antiferromagnetic ground state is realized due to a frustration-breaking trigonal-orthorhombic phase transition. For $R$ = Lu, however, a long-range ordered state has rarely, if ever, been reported despite a similar symmetry-breaking transition, albeit at a significantly lower temperature. To explore this dichotomy, we present a comprehensive magnetic and structural phase diagram for $Y_{1-x}Lu_xBaCo_4O_7$, established through complementary neutron diffraction and magnetization measurements. Our results outline the phase evolution of the nuclear structures in response to changes in composition and temperature. The temperature of the trigonal ($P31c$) to orthorhombic ($Pbn2_1$) transition, $T_{s1}$, decreases monotonically with increasing Lu content from 310 K for $x = 0.0$ to 110 K for $x = 1.0$. In Lu-rich compositions ($0.7 \leqslant x \leqslant 1.0$), first-order structural transitions are observed with coexisting and competing orthorhombic $Pbn2_1$ and metastable monoclinic $Cc$ phases. For the magnetically ordered Y-rich compositions, $T$- and $x$-dependent refinements of the magnetic structure reveal an antiferromagnetic "ribbonlike" arrangement of Co spin pairs in both the triangular and the kagome layers. A gradual suppression of long-range magnetic order is observed with increasing the Lu content, accompanied by the development of short-range magnetic correlations present in all the samples.

## I. INTRODUCTION

Geometrically frustrated systems represent a unique class of materials in which the configuration of magnetic moments on the crystal lattice leads to suppression of long-range magnetic order. This frustration arises from an inherent mismatch between magnetic interactions and lattice geometry, preventing the establishment of a unique ground state due to the impossibility of satisfying all interactions simultaneously. Various lattice geometries such as triangular, kagome, and pyrochlore lattices [1–11] are associated with geometric frustration. A characteristic feature of these materials is the persisting absence of a conventional ordered magnetic state, even at the lowest temperatures. Instead, observations often reveal the presence of short-range or spin-liquid-like correlations.

The family of $R$BaCo₄O₇ cobaltites, denoted as $R$-114 [with $R$ = Ca, In, Y, or a rare earth ($RE$) element] serves as a model system for investigating competing short-range (SRO) and long-range (LRO) magnetic orders resulting from geometric frustration within a trigonal structural framework. The trigonal structure is best described as a stack of alternating two-dimensional kagome and triangular layers, with the layers comprising cobalt ions occupying the center of corner-shared

oxygen tetrahedra, as illustrated in Fig. 1. The stacking of the triangular layers follows an $\cdots$ AAA $\cdots$ sequence. This can be compared to the pyrochlore lattice, which shares a motif of alternating kagome and triangular layers, but for which the stacking sequence is $\cdots$ ABC $\cdots$. For $R$-114, the $\cdots$ AAAA $\cdots$ stacking sequence leads to a transition metal sublattice comprising columns of trigonal biprisms along the $c$ axis. Charge balance necessitates the presence of a mixed Co oxidation state, with $Co^{2+}$ and $Co^{3+}$ ions apparently randomly distributed among the tetrahedral centers of two independent sites. For compositions with a trivalent $R$ ion [i.e., $R$ = In, Y, or a rare earth ($RE$) element], an average Co oxidation state of 2.25+ is expected, along with a 3:1 $Co^{2+}/Co^{3+}$ ratio. In the case of Ca-114 (where $R$ is a divalent ion), an equal number of $Co^{2+}$ and $Co^{3+}$ ions are present in a 1:1 ratio, owing to the average Co oxidation state increasing to 2.5+ [12–15].

$R$-114 materials undergo a first-order trigonal $P31c$ to orthorhombic $Pbn2_1$ structural phase transition at a temperature denoted as $T_{s1}$. This transition occurs slightly above room temperature for large $R$ ions and decreases to values near or below room temperature depending on the specific identity of $R$. The mechanism responsible for this transition, which breaks the threefold rotational symmetry of the trigonal structure, has been linked to the temperature-dependent behavior of severely underbonded Ba ions [16], to disruption of close-packed anion layers [17], or potentially to charge redistribution of the Co ions [18,19]. Irrespective of the origin of the phase transition,

---
*Present address: Department of Physics Engineering, Istanbul Technical University, Istanbul 34467, Turkey.
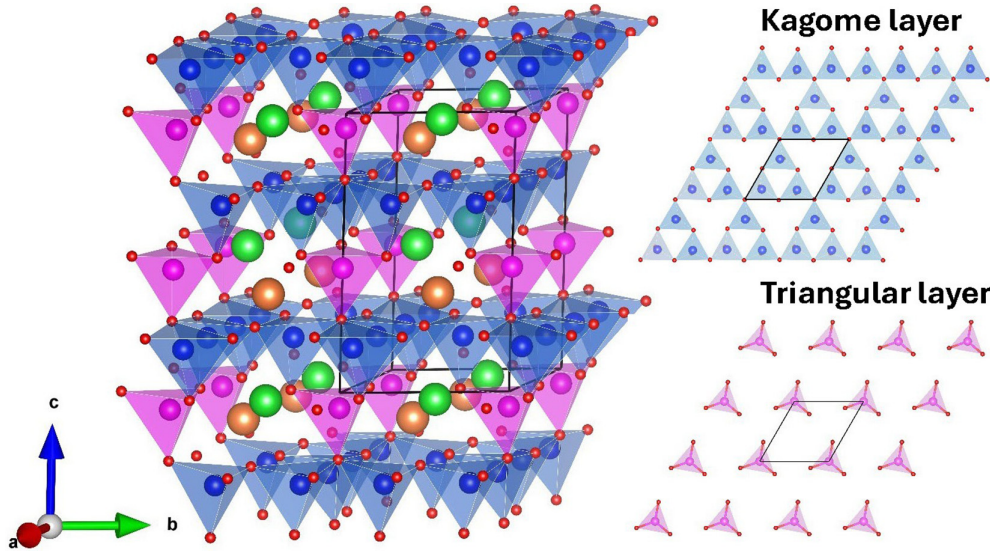
FIG. 1. Crystal structure of the $R$BaCo$_4$O$_7$ family with the trigonal symmetry of space group $P31c$. Cobalt atoms occupy the centers of the polyhedra shown in the kagome and triangular layers. Oxygen, barium, and $R$ atoms are represented by the red, green, and orange spheres, respectively.

$T_{s1}$ displays a linear dependence on the ionic radius of the $R^{3+}$ cation [17].

On the other hand, the $R$-114 system exhibits various magnetic properties at temperatures below 100 K, strongly influenced by the choice of the $R$ cation. Magnetization and magnetic relaxation measurements reveal spin-glass-like freezing behavior in InBaCo$_4$O$_7$ [20], for example, while clear ferrimagnetic order below 70 K is found in CaBaCo$_4$O$_7$ [21,22]. YBaCo$_4$O$_7$ exhibits fast decaying spin-spin correlations indicative of spin liquid properties [23], coupled with long-range antiferromagnetic (AFM) ordering below 106 K ($T_N$). Spin reorientation below 50 K is suggested by neutron diffraction [13,24].

Combining neutron powder and single crystal diffraction, Chapon *et al.* [13] and Khalyavin *et al.* [24] proposed two slightly modified magnetic ordering models for YBaCo$_4$O$_7$ using the Shubnikov magnetic space group $P2'_1$, with the main difference being an out of plane component allowed for the Co spins in the kagome layers [24]. Conversely, Hoch *et al.* [25], using $^{59}$Co NMR, suggested an ordering in which the Co magnetic moments in the triangular layer are similar to the neutron diffraction model, while those in the kagome layer all lie within the $ab$ plane and form a different pattern. In addition to the long-range magnetic order observed in Y-114 single crystals, the presence of significant short-range magnetic correlations below 250 K [13] was suggested, with these correlations persisting down to 2 K [24].

In prior research, we documented the observation of two successive first-order phase transitions in Lu-114, with the observed low-temperature phase depending on the cooling speed to base temperatures. Extremely fast cooling (3.5 K/min or more) was observed [12] to suppress the low temperature orthorhombic $Pbn2_1$ structure, allowing the transition from the trigonal $P31c$ symmetry to proceed directly to a metastable monoclinic $Cc$ phase below 160 K, which remains the observed phase down to 2 K. Cooling rates slower than this proved inadequate in removing the latent heat of this transition

swiftly enough to suppress the orthorhombic phase, resulting in coexisting orthorhombic and monoclinic phases, with varying phase fractions dependent on the cooling rate [12]. The intermediate monoclinic phase seems to be unique to Lu-114 and has rarely, if ever, been observed in other $R$-114 systems. Additionally, no long-range magnetic ordering is observed in Lu-114 [12,14], except for broad diffuse magnetic scattering intensities appearing at low temperatures after a waiting time of at least 30 min, indicating short-range magnetic correlations below $\approx$95 K [12].

The distinct structural and magnetic features of the Y and Lu members of the $R$-114 family have motivated us to explore the entire Y$_{1-x}$Lu$_x$BaCo$_4$O$_7$ solid solution system. Our goal is to understand how lattice and spin order evolve across the series. In this study, we present a comprehensive phase diagram for Y$_{1-x}$Lu$_x$BaCo$_4$O$_7$, revealing a crossover from long-range magnetic ordering to short-range magnetic correlations as the Lu content increases. The temperature of the trigonal to orthorhombic structural transition, $T_{s1}$, progressively decreases with the increasing Lu concentration. The metastable $Cc$ phase is exclusively observed in compositions where $0.7 \leqslant x \leqslant 1.0$. On the Y-rich side of the phase diagram, Rietveld refinement reveals antiferromagnetic coupling of four cobalt spin pairs in both the kagome and the triangular layers, with their directions confined to the $ab$ plane. Within each kagome triangle, two spins exhibit ferromagnetic coupling, while the others are coupled antiferromagnetically, forming what resembles "ribbons" along one of the unit cell's $ab$ plane diagonals. Magnetic short-range correlations are observed in all samples with their magnitude gradually increasing as the Lu content rises.

## II. EXPERIMENTAL DETAILS

Solid solutions of Y$_{1-x}$Lu$_x$BaCo$_4$O$_7$ with $\Delta x$ intervals of 0.1 were synthesized using conventional solid-state methods. To eliminate moisture from Y$_2$O$_3$ and BaCO$_3$ precursors, the

powders were dried separately, with $Y_2O_3$ dried overnight at $1000\,^{\circ}\text{C}$ in flowing oxygen and $BaCO_3$ in a box oven at $180\,^{\circ}\text{C}$. High-purity powders of $Lu_2O_3$ (99.999%), $Y_2O_3$ (99.995%), $Co_3O_4$ (99.99%), and $BaCO_3$ (99.99%) were combined in stoichiometric ratios. The mixtures underwent sintering in air at $1000\,^{\circ}\text{C}$, $1050\,^{\circ}\text{C}$, and $1150\,^{\circ}\text{C}$ in successive 24 h cycles, with intermediate grindings. At the conclusion of the final sintering cycle, the samples were rapidly quenched to room temperature and subsequently annealed at $600\,^{\circ}\text{C}$ (873 K) for 12 h under argon, resulting in the formation of the final stoichiometric $Y_{1-x}Lu_xBaCo_4O_{7.0}$ phases.

Magnetic susceptibility measurements were conducted on powder samples enclosed in small gelatin capsules utilizing a Quantum Design PPMS magnetometer (Quantum Design, San Diego, CA, USA). Samples were measured using zero-field-cooled on warming (ZFC-W), field-cooled on cooling (FC-C), and field-cooled on warming (FC-W) protocols, all conducted under a magnetic field of 1 T. Dc magnetization measurements were performed during both the warming and cooling processes at a rate of 2 K/min.

High-resolution neutron powder diffraction data were collected using the time of flight (TOF) diffractometer POW-GEN [26] at the Spallation Neutron Source, Oak Ridge National Laboratory. Temperature-dependent data for the Lu-substituted samples were collected in two frames with wavelengths centered at $1.066\,\text{Å}$ (the analyzed $Q$-space data spans between 1.965 and $19.626\,\text{Å}^{-1}$) and $3.731\,\text{Å}$ ($Q$-space data range from 0.753 to $3.733\,\text{Å}^{-1}$), while data for $YBaCo_4O_7$ were collected in a single frame with a center wavelength of $1.5\,\text{Å}$ ($Q$-space data range from 0.531 to $12.30\,\text{Å}^{-1}$). Data in the neutron diffraction experiments were collected on warming. Due to limited beam time, temperature-dependent neutron data for the $x = 0.3$ sample were not collected; instead, data were only recorded at 12 K for this composition.

To account for the metastable $Cc$ phase fraction's dependence on the cooling rate, with the highest fraction achieved by fast cooling, samples were cooled as rapidly as possible to base temperature using POWGEN's automatic sample changer. This process typically took about 80 min to reach 12 K, at an average rate of 3.5 K/min. For $LuBaCo_4O_7$, this average cooling rate was previously demonstrated to be sufficient for achieving 100% phase conversion to the metastable monoclinic $Cc$ phase for samples of typical mass for neutron diffraction [12].

Nuclear and magnetic structures were determined using Rietveld refinement methods as implemented in the General Structure Analysis System (GSAS II) [27,28]. Nuclear structural models were plotted using VESTA [29].

### III. RESULTS AND DISCUSSION

#### A. Phase diagram

Using neutron diffraction and dc magnetometry, we mapped the relationship among structural and magnetic phases for the $Y_{1-x}Lu_xBaCo_4O_7$ series, as shown in Fig. 2, which is drawn to convey the equilibrium situation where the $Pbn2_1$ phase is the ground-state phase below $T_{s1}$ for $x \geqslant 0.7$. As mentioned above and detailed below, the $Cc$ phase can
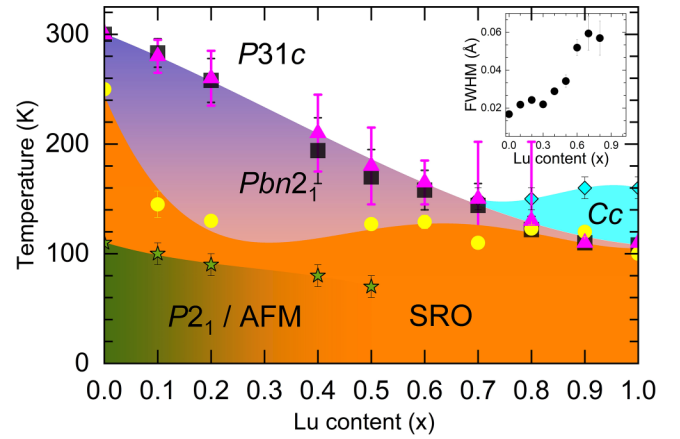


FIG. 2. Proposed equilibrium structural and magnetic phase diagram of $Y_{1-x}Lu_xBaCo_4O_7$ ($\Delta x = 0.1$). The black squares indicate the structural transition temperatures obtained from the first derivatives of the magnetization vs temperature curves, with error bars corresponding to the width of the peak on the first derivatives. The magenta triangles represent the structural transition temperatures ($T_{s1}$) to orthorhombic $Pbn2_1$, obtained from neutron diffraction data. The error bars on the magenta triangles indicate the biphasic region where trigonal and orthorhombic phases coexist in various amounts. The green stars denote the transition temperatures of long-range ordered antiferromagnetic structures (LRO AFM) obtained from neutron diffraction data. Cyan diamonds mark the structural transition temperatures ($T_{s2}$) to the monoclinic $Cc$ phase. The error bars on the cyan diamonds and green stars are set to 10 K, as the neutron data were collected with 10 K intervals. Yellow circles represent the onset of short-range magnetic correlations (SRO), with data for $x = 0.0$ and $x = 1.0$ taken from Refs. [12,13], respectively. The error bars on the yellow circles for $0.1 \leqslant x \leqslant 0.9$ are determined from the sigmoidal function fit to the integrated intensity of the (012) magnetic reflection (see Fig. 3). The borders of the violet (orthorhombic $Pbn2_1$ phase), cyan ($Cc$ phase), green (AFM), and orange (SRO) regions are guides to the eye obtained by polynomial fits to the corresponding data points from neutron diffraction. Inset: Full width at half maximum (FWHM) of the (012) magnetic peak as a function of Lu content. Neutron diffraction data for the $x = 0.0$ sample are collected at 5 K, for the rest of the samples at 12 K.

be supercooled. Thus diffraction data (for example, see Fig. 6 and the relevant text) often show persistence of this metastable phase because cooling was not sufficiently slow. A "metastable phase diagram" that captures this behavior is shown in Supplemental Material Fig. 1 in the Supplemental Material (SM) [30]. Despite this complication, the evidence presented here is consistent with the $Pbn2_1$ phase as the ground state for all $x$.

Consistent with earlier findings, the 300 K structure of $YBaCo_4O_7$ is orthorhombic, undergoing a structural transition from the trigonal symmetry slightly above room temperature [13]. We have previously suggested that this transition, also observed in $YbBaCo_4O_7$, is driven by underbonding of the $Ba^{2+}$ ion [16]. Subsequently, it has been shown that substitution on the rare earth ($R$) site can influence the transition temperature, with smaller $R$ leading to reduced $T_s$ (please see, for example, Fig. 2 in Ref. [17]). These authors attribute the $R^{3+}$ size effect as arising from destruction of close
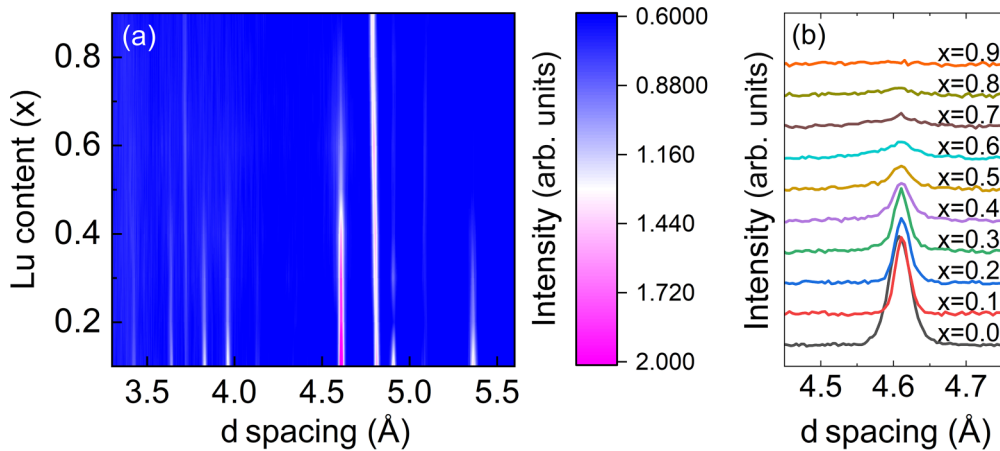
FIG. 3. (a) Color map displaying a portion of the neutron diffraction data for $Y_{1-x}Lu_xBaCo_4O_7$ and highlighting the suppression of magnetic peaks with increasing Lu content. (b) The 012 magnetic reflection for each sample at 5 K for $x = 0.0$, 10 K for $x = 1.0$, and 12 K for the other Lu-substituted samples. The measurements were conducted on warming after fast cooling at a rate of $\approx 3.5$ K/min, as outlined in the experimental details. Under these conditions, the low-temperature symmetry of the predominant phase is $Pbn2_1$ for $0 \leqslant x \leqslant 0.8$ and $Cc$ for $0.9 \leqslant x \leqslant 1$.

packed stacking of the $BaO_3$ and $O_4$ layers in the hexagonal high-temperature phase. Smaller $R^{3+}$ ions are shown by these authors to exhibit a $c/a$ ratio very close to the ideal for close packed layers and so will stabilize the hexagonal phase to lower temperatures. In contrast, larger $R^{3+}$ ions (beyond $\sim 0.9$ Å radius) exhibit a $c/a$ ratio markedly deviating from close packed and so the transition occurs at higher temperature. Substituting Lu for Y continuously suppresses the transition temperature, denoted $T_{s1}$, down to 110 K (for $x = 1$). In all Lu-substituted samples, the room temperature structure falls within the trigonal phase regime.

The values of $T_{s1}$, determined through zero-magnetic-field neutron diffraction and Rietveld refinements (depicted as magenta triangles in Fig. 2), align well with those extracted from first derivatives of the magnetization curves (represented by black squares in Fig. 2), despite the latter measurements being under 1 T magnetic fields. The light violet region in the phase diagram delineates the equilibrium-state orthorhombic $Pbn2_1$ phase. On the Lu-rich side of the phase diagram ($0.7 \leqslant x \leqslant 1.0$), two successive structural transitions to monoclinic $Cc$, denoted $T_{s2}$, and then to orthorhombic $Pbn2_1$ at $T_{s1}$, are observed.

As mentioned earlier, oxygen stoichiometric $YBaCo_4O_{7.0}$ exhibits a long-range ordered magnetic structure below 110 K ($T_N$) [13]. A slight increase in oxygen content, as in $YBaCo_4O_{7.1}$, for example, completely suppresses both the nuclear and magnetic transitions with the structure remaining trigonal down to the lowest measured temperature at 6 K [31]. Sharp and intense magnetic peaks shown in Fig. 3 and Supplemental Material Fig. 2 [30] provide strong evidence for the full and exact oxygen stoichiometry (i.e., 7.0 oxygen atoms per formula unit) in our Y-rich compositions.

As shown in Fig. 2, Lu substitution progressively reduces the onset of the magnetic transition temperature to 70 K for compositions with $x$ up to 0.5. Samples with $x > 0.5$ exhibit no long-range magnetic order, which is suppressed in favor of short-range magnetic correlations, as seen in the neutron diffraction data displayed in Fig. 3(b), for example. Short-range magnetic correlations manifest as diffuse

scattering intensities at $\approx 120$ K and below for the $x = 0.0$ sample (Supplemental Material Fig. 2 [30]) and below $\approx 100$ K for all Lu-substituted samples, including those displaying long-range magnetic order.

Due to relatively coarse substitution increments ($\Delta x = 0.1$) in our solid solution materials, the exact composition between $x = 0.5$ and 0.6 at which the transition from long-range to short-range correlations occurs, both in terms of temperature and Lu content, cannot be precisely determined. Nevertheless, reasonable magnetic structural refinements at 12 K were performed for the $x \leqslant 0.5$ samples, despite the gradual and fast suppression (Fig. 3) and broadening of the magnetic peaks as Lu content increased (see inset of Fig. 2).

On the other hand, the onset of short-range magnetic order (SRO) was determined by fitting temperature-dependent integrated intensities of several magnetic reflections as shown in Fig. 4, for example. A sigmoidal function (solid red curves) was used for fitting, and the second derivatives of the fits (insets in Fig. 4) were used to determine the inflection points corresponding to the onset of SRO in our bulk polycrystalline materials. Further insights into short-range magnetic correlations, beyond the scope of this paper, would necessitate inelastic and quasielastic neutron measurements from single crystals.

### B. Structural properties

Our phase diagram (Fig. 2) comprehensively delineates most of the known nuclear phases in the $R$-114 system. However, we did not observe evidence for the low-temperature monoclinic phase ($P2_1$) on the Y side, which has been reported for $YBaCo_4O_7$ [13,24] and identified by a peak splitting of the nuclear (221) reflection using high-resolution synchrotron x-ray diffraction. Our neutron diffraction data are of insufficient resolution to observe this peak splitting. As a result, attempts to perform meaningful nuclear structure Rietveld refinements using the $P2_1$ symmetry were not possible, due to the low symmetry requiring 25 independent atoms with three degrees of freedom each. Therefore, our nuclear
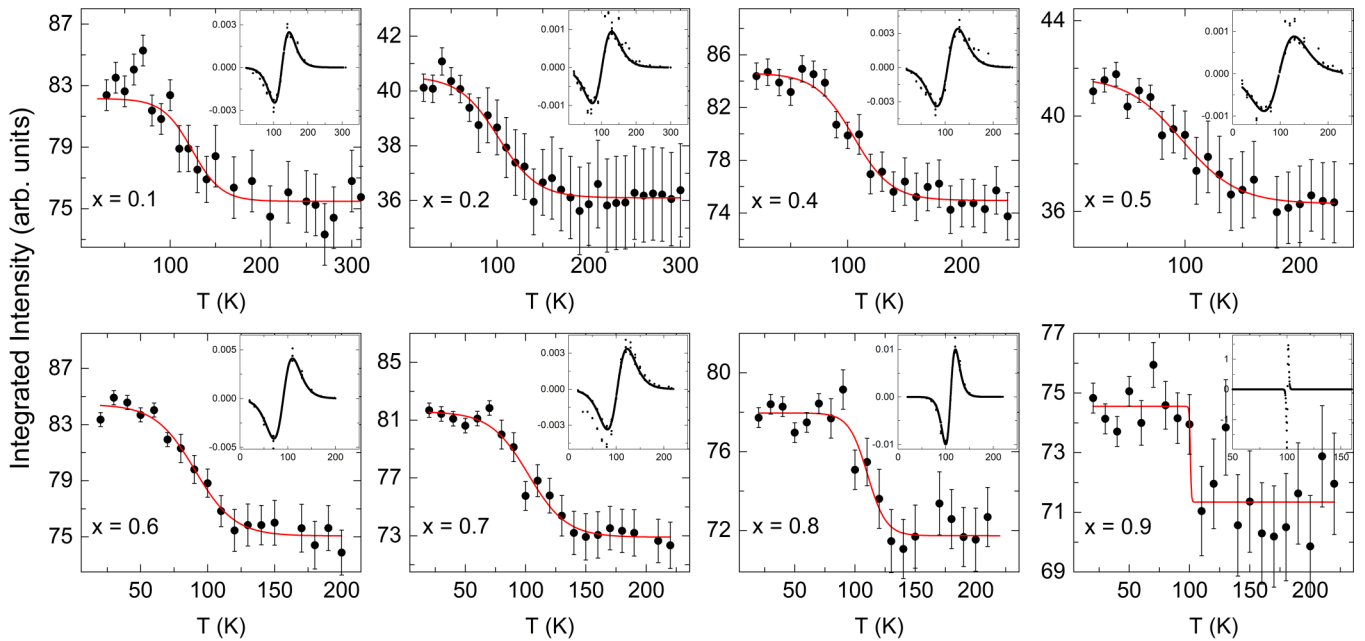
FIG. 4. Integrated intensities represented by black closed circles of the (012) magnetic reflection for samples with $0.1 \leqslant x \leqslant 0.9$ samples. The solid red lines depict sigmoidal function fits to the data. Insets show the second derivatives of the sigmoidal function fits as a function of temperature. The neutron diffraction data were collected during the warming phase after fast cooling at a rate of $\approx 3.5$ K/min down to 12 K.

structural refinements were conducted using an orthorhombic $Pbn2_1$ model between $T_{s1}$ and 12 K.

Due to the first-order nature of the $P31c$-$Pbn2_1$ structural phase transition, samples with $0.1 \leqslant x \leqslant 0.7$ exhibit biphasic behavior in the vicinity of $T_{s1}$. Two-phase refinements were conducted to characterize this coexistence, as reflected in the relatively large coexistence range represented as "error" bars over the magenta triangles on the phase diagram. A color map displayed in Fig. 5 illustrates this phase coexistence during
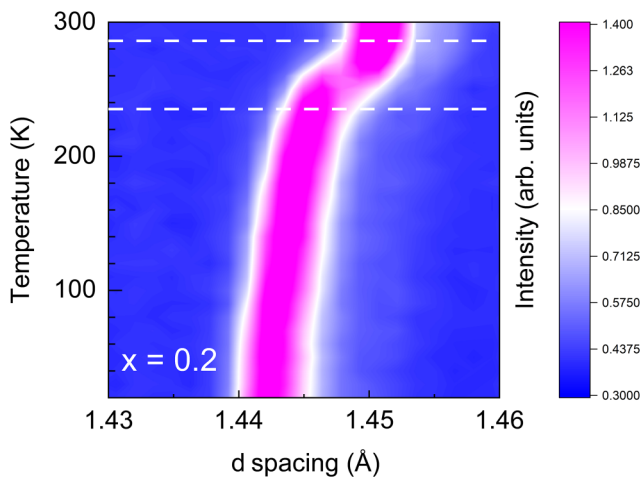


FIG. 5. A portion of neutron diffraction data for the $x = 0.2$ sample illustrating the structural transition from trigonal to orthorhombic phases. The biphasic region between the two horizontal dashed lines indicates the coexistence of both phases. The neutron diffraction data were collected during the warming phase after fast cooling at a rate of $\approx 3.5$ K/min down to 12 K.

the phase transition, with additional plots for other samples displayed in Supplemental Material Fig. 3 [30].

Similar to LuBaCo$_4$O$_7$ [12], regions exhibiting biphasic and single-phase monoclinic $Cc$ structures are observed by neutron diffraction for samples with $x \geqslant 0.7$ when measured on warming, thus revealing the metastability of this phase. A single, monoclinic $Cc$ phase can be isolated in the $x = 1.0$ sample (LuBaCo$_4$O$_7$) at 12 K upon fast cooling [12]. However, employing the same fast-cooling protocol at the same instrument (POWGEN) for $x = 0.7$, 0.8, and 0.9 resulted in variable biphasic mixtures at 12 K, reflecting the nonequilibrium nature of the $Cc$ phase at low temperature. A color map for the $x = 0.9$ sample in Fig. 6(a) illustrates the temperature-dependent evolution of mixed $Cc$ and $Pbn2_1$ diffraction peaks at 1.565 Å (indexed as monoclinic [400]) and 1.57 Å (indexed as orthorhombic [145] and [253]), respectively. The intense middle peak represents overlapped reflections from both phases, merging into a single $Cc$ phase above $\approx 120$ K, followed by transition to trigonal $P31c$ (220) reflection at temperatures above $\approx 160$ K. No trace of the monoclinic $Cc$ phase was detected within the resolution limit of POWGEN in any of the remaining samples with $x \leqslant 0.6$. Additional neutron diffraction plots for $x = 0.7$ and 0.8 are shown in Supplemental Material Fig. 4 [30], along with the refined phase fractions by weight of the identified phases.

Multiple phases—$Cc$, $Pbn2_1$, and $P31c$—compete as a function of temperature, revealing their thermodynamic and kinetic stability regions. For example, consider the case of $x = 0.9$ where, despite the fast-cooling protocol designed to kinetically trap the $Cc$ phase, the sample still transformed significantly to $Pbn2_1$. Upon warming this metastable phase mixture, the weight fractions of the $Cc$ and $Pbn2_1$ remain relatively unchanged between 12 and $\approx 50$ K [region I in Fig. 6(b)]. We argue that the kinetic barrier between
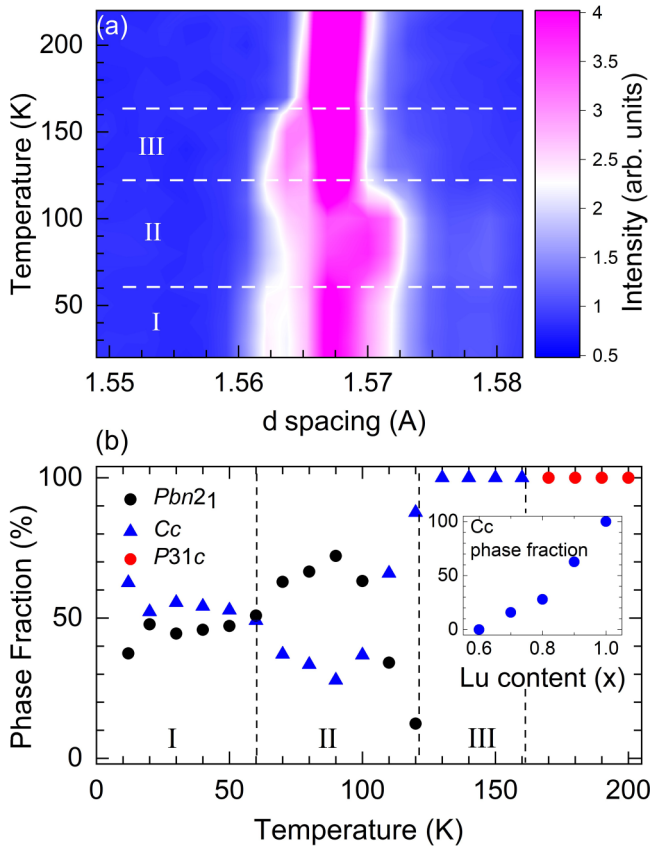
FIG. 6. (a) A Color map displaying a portion of neutron diffraction data for the $x = 0.9$ sample. (b) Calculated phase fractions of $Pbn2_1$ and $Cc$ phases for the $x = 0.9$ sample. Region III corresponds to a pure $Cc$ phase, while regions I and II indicate a mixture of $Pbn2_1$ and $Cc$ phases. In region I, the $Cc$ phase dominates, while in region II, $Pbn2_1$ is the dominant phase until it starts disappearing above 100 K. The inset displays the phase fraction of the $Cc$ phase as a function of Lu content at 12 K. The weight fraction of the orthorhombic $Pbn2_1$ phase exhibits an opposite trend. The data were collected during the warming phase after fast cooling at a rate of $\approx3.5$ K/min down to 12 K. Despite this rapid cooling process, a significant fraction of the high-temperature $Cc$ phase was converted to $Pbn2_1$.

metastable $Cc$ and the ground state $Pbn2_1$ is too high at these low temperatures to observe conversion on the measurement timescale. The $Pbn2_1$ phase gradually becomes dominant from $\approx50$ to $\approx100$ K (within region II), reflecting the onset of thermally induced (kinetic) conversion of the metastable $Cc$ phase to the thermodynamically stable $Pbn2_1$ phase. This behavior mirrors that of pure Lu-114 ($x = 1.0$) [12].

Upon further heating above $\approx100$ K, the phase fractions reverse trends as the system approaches the thermodynamic stability region of the $Cc$ phase near 120 K. The $Cc$ phase then remains present in a single-phase form, ultimately transitioning to the trigonal $P31c$ symmetry at $\approx160$ K. The inversely related $Cc$ and $Pbn2_1$ phase fractions change continuously with increasing Y content, as shown implicitly in the refined phase fraction behavior of the $Cc$ phase in the inset of Fig. 6(b). We note (Supplemental Material Fig. 4 [30]) that as might be expected, the phase fraction of supercooled $Cc$ becomes larger as $x$ nears 1.0. Finally, neutron diffraction
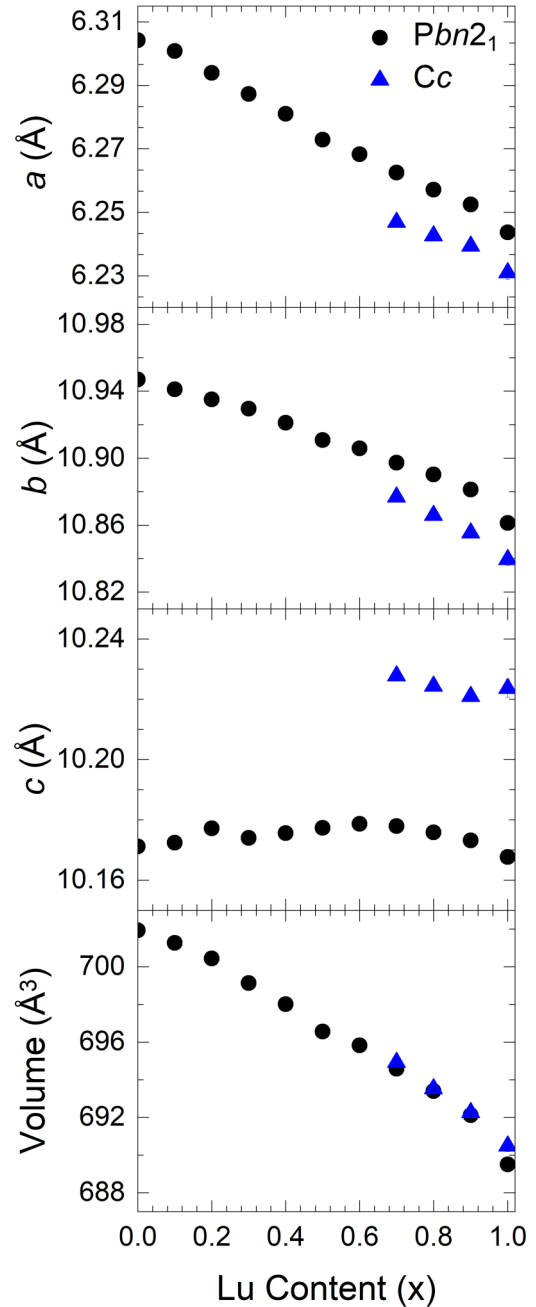


FIG. 7. Variations of the unit cell parameters as a function of Lu content at 12 K. Data points for $x = 1.0$ are taken from Ref. [12]. Error bars, smaller than the symbols, indicate the uncertainties associated with the measurements. The neutron diffraction data were collected during the warming phase after fast cooling at a rate of $\approx3.5$ K/min down to 12 K.

measurements in Ref. [12] show that extremely slow-cooled (0.1 K/min) samples of $x = 1.0$ led to almost 100% conversion to $Pbn2_1$. We suggest a similar behavior would be found here for the samples with $x \geqslant 0.7$ at similarly slow cooling rates. Structural models displaying the subtleties of the competing $Cc$ and $Pbn2_1$ phases are illustrated in Supplemental Material Fig. 5 [30].

The unit cell lattice parameters and unit cell volume at 12 K are shown in Fig. 7 as a function of Lu substitution. As
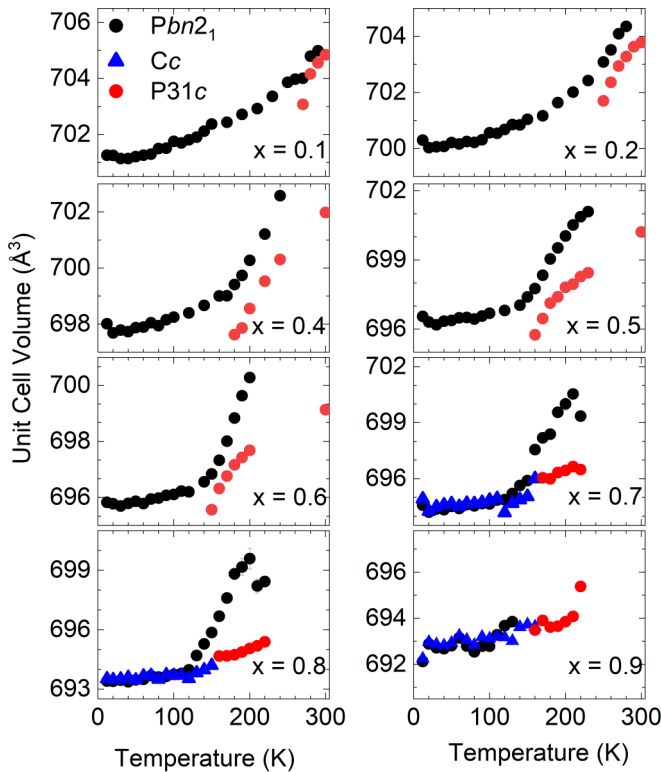
FIG. 8. Unit cell volume as a function of temperature for $Y_{1-x}Lu_xBaCo_4O_7$. For the $P31c$ phase, the unit cell volume was multiplied by a factor of 2. The error bars, smaller than the symbols, represent the uncertainties associated with the measurements. The neutron diffraction data were collected on warming after fast cooling at a rate of $\approx 3.5$ K/min down to 12 K.

predicted by Vegard's law [32], the linear contraction of the unit cell volume and the in-plane $a$ and $b$ lattice parameters arises from site-sharing six coordinated Y and Lu ions with contrasting ionic radii, where $r_Y = 0.90$ Å and $r_{Lu} = 0.861$ Å [33]. However, we argue that the nonlinear behavior of the $c$ lattice parameter in our layered $Y_{1-x}Lu_xBaCo_4O_7$ structure is likely due to preferential site occupancy of the substituting Lu ions, thus giving rise to anisotropic strains and disorder and producing a more pronounced effect on the in-plane lattice parameters compared with the direction perpendicular to the layers. It is worth noting that the full replacement of Y by the smaller Lu ion shrinks the unit cell volume by about 1.7%, bringing the ions closer together and increasing magnetic interactions. This reduction in volume also lowers the $P31c$ to $Pbn2_1$ transition temperature $T_{s1}$, below which short-range magnetic ordering first occurs, as observed in Y-114. These short-range correlations, combined with the approach to a region of thermodynamic metastability, involve evolving distortions that stabilize various phases, competing with a complex set of magnetic interactions. This interplay suppresses long-range magnetic order, potentially due to either persistent geometric frustration or enhanced exchange-driven frustration.

The evolution of the unit cell volume and unit cell lattice parameters as a function of temperature is illustrated in Fig. 8 and Supplemental Material Fig. 6 [30], respectively, for all

three nuclear phases observed in our samples. While the Y-rich compositions ($x = 0.1$ and 0.2) display typical thermal expansion behavior, $dV/dT > 0$, a clear inflection point at $\approx 120$ K is noticeable, starting with $x = 0.5$ for the $Pbn2_1$ unit cell volume (depicted by black circles). Below this temperature, the volume becomes nearly temperature independent. The response of the short $a$ axis to temperature is more pronounced, exhibiting negative thermal expansion behavior for the $x = 0.1$ and $x = 0.2$ samples. No changes are observed along the $b$-axis direction, and the self-compensated combination of all three parameters leads to the unit cell volume behavior shown in Fig. 8.

### C. Magnetic properties

The transition between trigonal and orthorhombic symmetries, while structurally driven, manifests as a kink in the magnetization data collected under a magnetic field of 1 T (see Fig. 9). This anomalous behavior, explained in previous work [16], is attributed to modified exchange interactions among the Co ions in response to a discontinuous rearrangement of the structure. Consistent with the gradual suppression of $T_{s1}$ observed in our neutron diffraction results, the kink shifts to lower temperatures and broadens with increasing Lu content.

The long-range AFM ordering for Y-rich compositions is subtly indicated by a change in slope at $\approx 100$ K in the magnetization data, collected under a cooling or warming rate of 2 K/min (Fig. 9), corresponding to the temperature where the magnetic peaks appear in the neutron data. A pronounced spin reorientation [13,24] hump observed at $\approx 50$ K in $YBaCo_4O_7$ broadens and shifts to lower temperatures with increasing Lu content before sharpening for samples with $x \geqslant 0.7$, as observed in the ZFC-W magnetization data, Fig. 9. This new sharp peak, unrelated to spin reorientation in the absence of long-range magnetic ordering, is found in samples where the metastable $Cc$ phase is observed during fast cooling. The sharp peak can be significantly suppressed with very slow cooling rates. Although cooling rate dependent measurements similar to those reported in [12] were not performed for our substituted samples, we note the distinct character of the peak—being sharp for fast-cooled Lu-rich samples and broad for Y-rich samples where long-range magnetic ordering and the $Pbn2_1$ phase dominate at low temperatures; see the inset of Fig. 6(b). When interpreted in the context of Ref. [12], this behavior implies that rapidly cooled samples with $x > 0.7$ develop short-range magnetic order in the metastable $Cc$ phase, signaled by the sharp peak, which subsequently "melts" upon warming into the $Pbn2_1$ phase in the 60–100 K range.

### D. Magnetic structures

The primary structural transition from trigonal to orthorhombic appears to be necessary to break the geometric frustration of the lattice and allow for potential long-range magnetic ordering at lower temperatures. The further lowering of the symmetry to monoclinic $P2_1$, lifting the magnetic ground-state degeneracy while preserving the translational symmetry of $Pbn2_1$, was reported [13,24] to occur simultaneously with the onset of magnetic ordering, indicative of strong magnetoelastic coupling. Furthermore, it should be
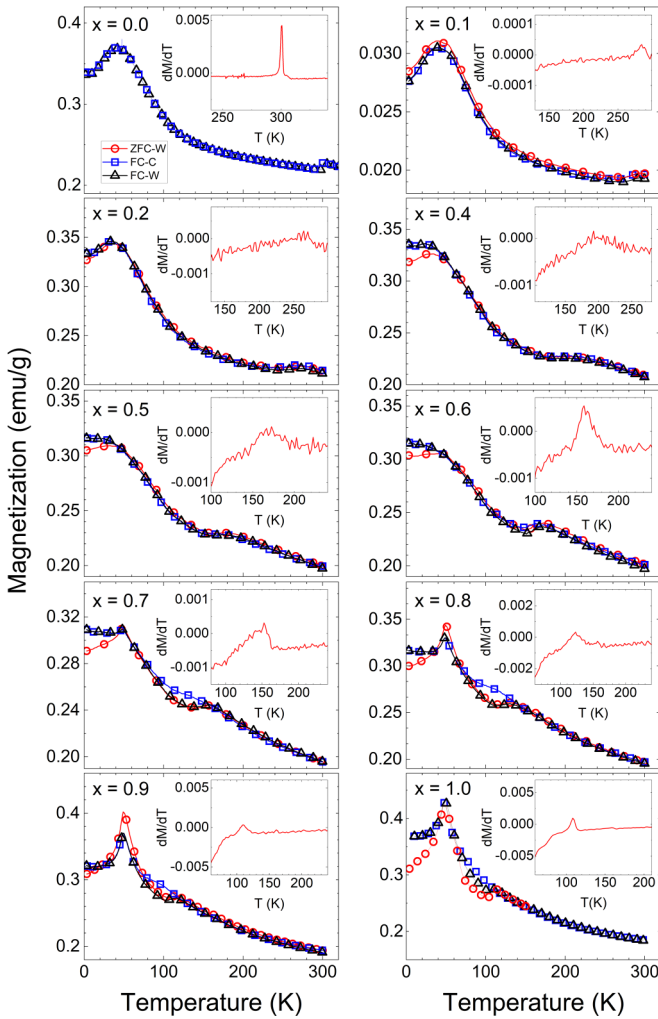
FIG. 9. Temperature dependence of magnetization for $Y_{1-x}Lu_xBaCo_4O_7$. The data were collected under a magnetic field of 1 T using various conditions: on warming after cooling in zero magnetic field (ZFC-W), on warming after cooling in a magnetic field (FC-W), and on cooling in a magnetic field (FC-C). The cooling and warming rate was set at 2 K/min. To enhance clarity, some data points are skipped. The insets show first derivatives of the corresponding magnetization data.

noted that suppression of the transition to orthorhombic symmetry on cooling in $YBaCo_4O_7$, for instance, by the addition of $\approx 1.5\%$ excess oxygen, prevents the subsequent transition at low temperature to long-range magnetic order. In this case, the minor crystallographic disorder introduced through the excess oxygen acts to defeat the symmetry breaking, thus preserving the geometric frustration, and leading to only short-range magnetic correlations [13,24]. Similarly, when two elements like Y and Lu with different ionic radii share the same crystallographic sites, they introduce significant disorder into the system. This disorder manifests intrinsically as strains and local distortions, and extrinsically as defects and domains of varying sizes. We hypothesize that this disorder is accountable for the continuous suppression of $T_{s1}$ and long-range magnetic order, thus maintaining geometric frustration and favoring short-range magnetic order.
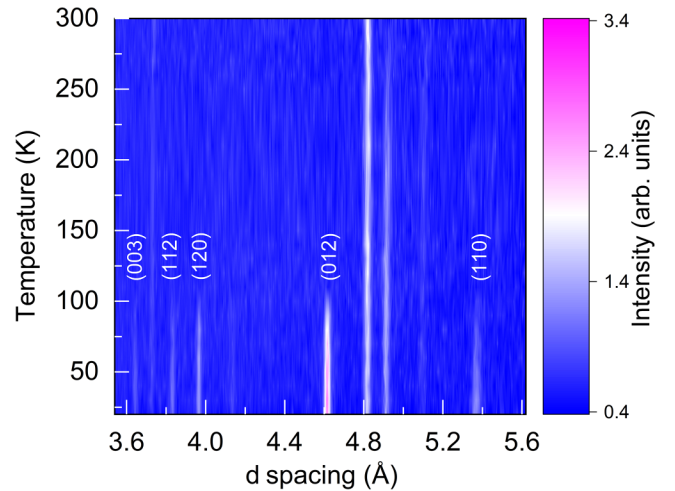


FIG. 10. Color map of neutron diffraction data for $x = 0.1$ sample as a function of temperature. Magnetic peaks (indexed) are observed below 100 K. The neutron diffraction data were collected on warming after fast cooling at a rate of $\approx 3.5$ K/min down to 12 K.

In the Y-rich samples ($0 \leqslant x \leqslant 0.5$), strong long-range magnetic peaks are observed at $d$ spacings $\approx 5.36$, 4.61, 3.96, 3.83, 3.64, and 3.21 Å (see Fig. 3) consistent with those reported in Ref. [24]. The continuous enhancement of short-range magnetic correlations, at the expense of suppressed long-range order, is reflected in the weakened peak intensities with increasing Lu content. Two additional magnetic peaks at 6.3 Å (100 reflection) and 7.4 Å (011 reflection) are specific to the $x = 0.0$ sample. Even a minimal 10% Lu substitution at the Y site is enough to suppress these two peaks, as shown in the Supplemental Material Fig. 7 [30]. Thus the magnetic structure of the Y-only sample may differ from that of the Lu-substituted ones, until only broad magnetic diffuse scattering intensities are observed around 4.6 Å for $x > 0.5$; see Fig. 3.

Figure 10 presents a limited range of neutron diffraction data for $x = 0.1$, highlighting several magnetic peaks below 100 K. Additional neutron diffraction data for $x = 0.2$, 0.4, 0.5, and 0.6 are shown in the Supplemental Material Figs. 8 and 9 [30]. Group theory calculations using $Pbn2_1$ and the propagation vector $k = (0, 0, 0)$ on the Bilbao Crystallographic server integrated with GSAS II resulted in 11 possible magnetic space groups with the Shubnikov symmetry notations $Pb'n'2_1$, $Pb'n2'_1$, $Pbn'2'_1$, $Pbn2_1$, $Pc'$, $Pn'$, $Pc$, $Pn$, $P2'_1$, $P2_1$, and $P1$ in which the primes correspond to time reversal symmetry operations. The magnetic peaks can all be indexed using the first four high-symmetry orthorhombic magnetic space groups; however, their calculated intensities were inadequate and resulted in poor fits. All the remaining monoclinic space groups, except $P2'_1$, were equally unsatisfactory. It is worth noting that $P2'_1$ is the same space group suggested in the literature [13,24]; however, as will be discussed below, our magnetic ordering model is significantly different. In our final refinements, the nuclear orthorhombic $Pbn2_1$ and monoclinic $P2'_1$ space groups were used for refinements of the nuclear and magnetic structures, respectively.

Magnetic refinements were initiated with no constraints on the magnetic moments of the eight cobalt atoms defined by $P2'_1$. In the initial refinement process, the symmetry-allowed

TABLE I. Atom positions of cobalt (Co) atoms in the magnetic phase at 5 K for the $x = 0$ sample.

| Atom | Color | $x$ | $y$ | $z$ |
|------|-------|-----|-----|-----|
| Co1 | Dark blue | 0.005(2) | 0.003(1) | 0.0617(6) |
| Co2 | Dark Blue | 0.495(2) | 0.503(1) | 0.0617(6) |
| Co3 | Green | 0.006(2) | 0.1721(7) | 0.314(1) |
| Co4 | Green | 0.494(2) | 0.6721(7) | 0.314(1) |
| Co5 | Purple | 0.258(2) | 0.0856(7) | 0.8105(8) |
| Co6 | Purple | 0.245(1) | 0.4180(7) | 0.3190(7) |
| Co7 | Cyan | 0.242(2) | 0.5856(7) | 0.8105(8) |
| Co8 | Cyan | 0.255(1) | 0.9180(7) | 0.3190(7) |

Cartesian coordinate components ($M_x$, $M_y$, $M_z$) of the magnetic moments were freely refined, starting from unbiased values deemed reasonable. However, negligible $M_z$ components were observed for all samples and temperatures during stable refinement cycles. Consequently, these out of plane components were fixed at zero during the final refinement cycles. Additionally, the refined magnetic moments of specific cobalt pairs (Co1 and Co2 in the triangular layer, and Co3 and Co4, Co5 and Co6, and Co7 and Co8 in the kagome layer) displayed a strong tendency to couple antiferromagnetically. To reflect this tendency, constraints were applied accordingly.

Table I provides the Co atomic positions for $x = 0$ at 5 K and the final magnetic structures at 10–12 K are displayed in Fig. 11. Notably, our refined model differs from the published models for $x = 0.0$ [24] in two key aspects: first, the magnetic moments on the kagome layer's cobalt ions were refined freely with no constraints to be equal, and second, various Co pairs tend to align antiferromagnetically, particularly the Co7-Co8 (cyan spheres) and Co3-Co4 (green spheres) pairs, giving rise to a distinctive "ribbonlike" appearance along the [1$\bar{1}$0] direction. Representative best-fit Rietveld refinement plots are shown in Fig. 12 for the $x = 0$, 0.2, 0.4, and 0.9 samples with additional plots and structural refinement results displayed in

Supplemental Material Figs. 10–12 and Supplemental Material Tables I–III, respectively [30].

Magnetic refinements for the $x = 0.0$ sample resulted in two slightly different models (A and B) at 5 K that are visually indistinguishable from a fit inspection or examination of the similar agreement factors of the refinements. Interestingly, this is the only sample for which the refinements converged to two different solutions. Model A, as illustrated in the Supplemental Material Figs. 13(a) and 13(b) [30], agrees with the structures obtained at 12 K for $x = 0.1$ and $x = 0.2$, whereas model B shows the spins of the Co3-Co4 pairs rotated in a direction "symmetrical" to that of model A with everything else remaining roughly similar; see Supplemental Material Figs. 13(c) and 13(d) [30]. However, when these two models were imposed on the Lu-substituted samples, a consistent and "unique" solution was always obtained, as described above and shown in Figs. 11 and 12. The robustness of our final magnetic models was evidenced by the similar solutions obtained for all the long-range magnetically ordered samples irrespective of the initial magnetic moment values. Attempts using constraints as in the published models [13,24,25] resulted in poor fits (see Supplemental Material Fig. 14 [30]), but releasing these constraints produced the same magnetic structures as those shown in Fig. 11.

Stable Rietveld refinements were achieved for all $x \leqslant 0.5$ samples at 12 K. The temperature evolution of Co magnetic ordering for $x = 0.1$ and 0.2 in the kagome and triangular layers is shown in Fig. 13 and the Supplemental Material Fig. 15 [30], respectively. The $x = 0.4$ and 0.5 samples exhibit small long-range ordered magnetic moments at 12 K, diminishing rapidly with increasing temperature, hindering meaningful refinements of temperature-dependent magnetic structures. The gradual suppression and broadening of magnetic peak intensities, coupled with relatively coarse $\Delta x = 0.1$ increments, make it difficult to delineate a clear boundary between long-range magnetic order and short-range correlations as a
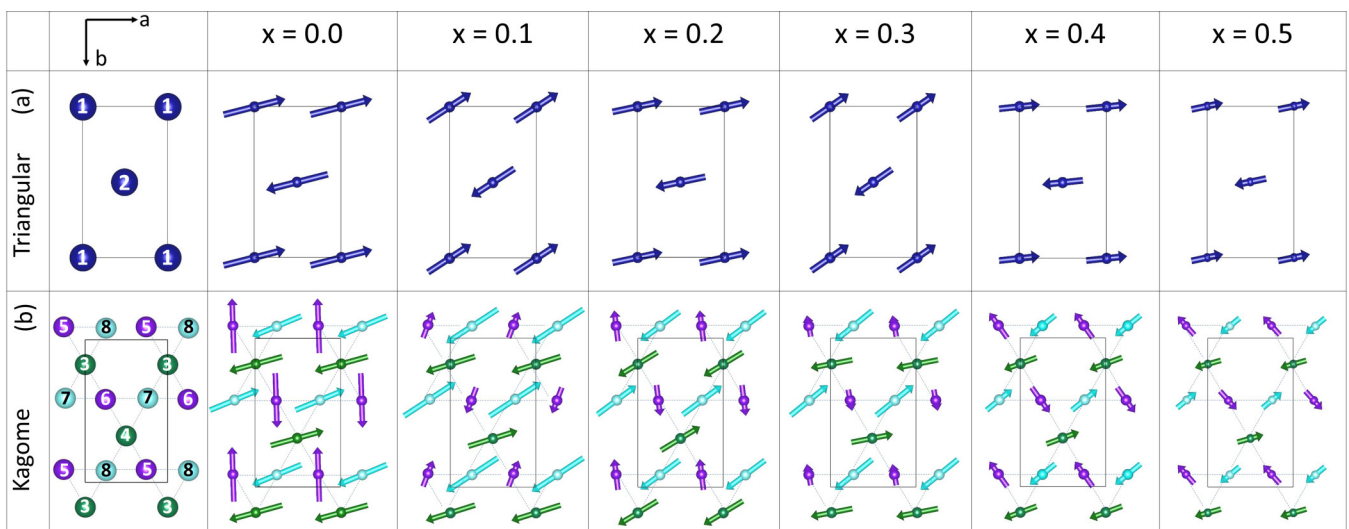


FIG. 11. Magnetic structures of long-range ordered Y$_{1-x}$Lu$_x$BaCo$_4$O$_7$ at 5 K for $x = 0.0$ and at 12 K for the Lu-substituted samples in both the triangular layer (a) and kagome layer (b). In the triangular layer, the antiferromagnetically coupled Co1-Co2 atom pairs are colored blue, while in the kagome layer, Co3-Co4 pairs are green, Co5-Co6 pairs are purple, and Co7-Co8 pairs are cyan. The arrows represent the relative magnetic moments, all lying in the $ab$ plane.
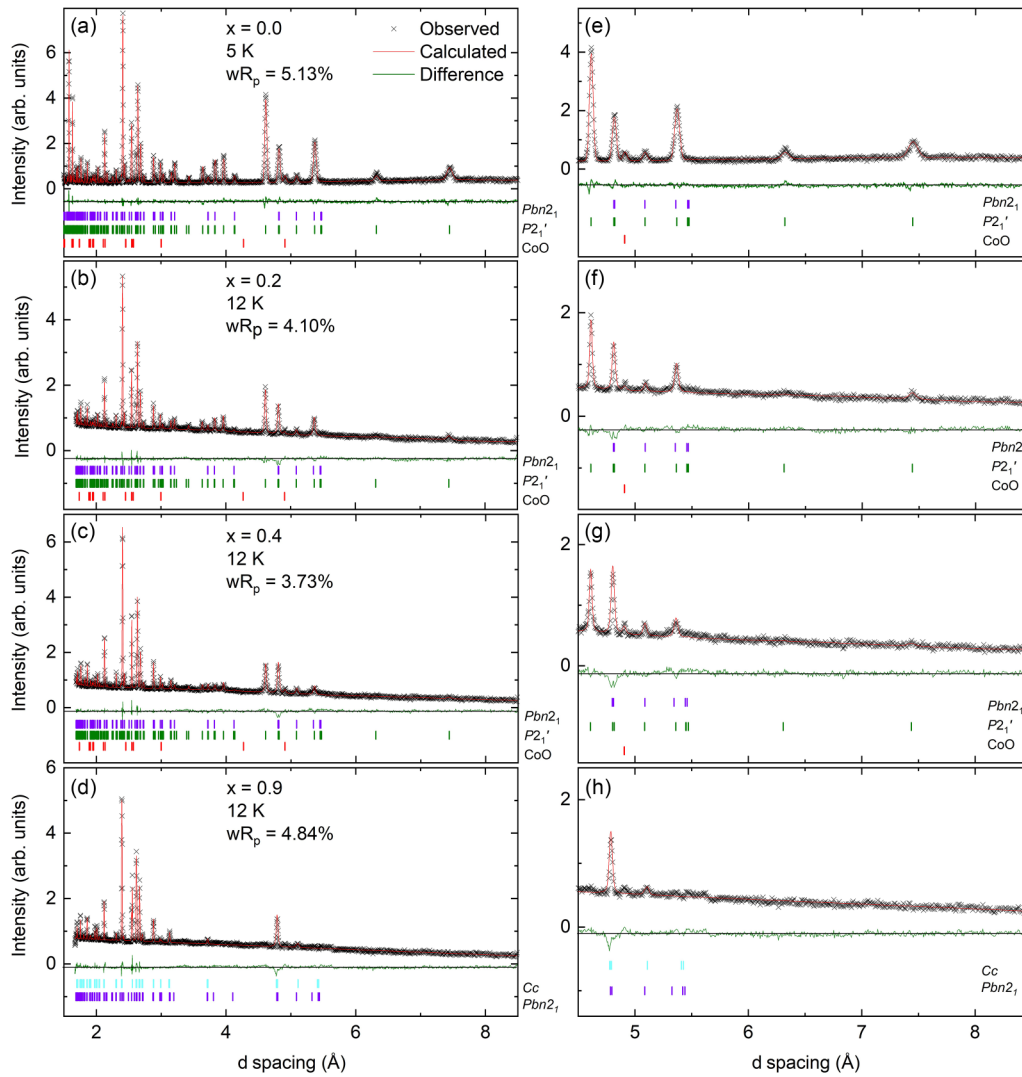
FIG. 12. Best-fit Rietveld refinement plots (a)–(d) showing the observed (black cross signs) and calculated (red lines) intensities together with their difference (green line under the peaks). Tick marks, under the intensity difference plots, represent the nuclear and magnetic Bragg peak positions of the indicated phases. Data were collected at base temperatures of 5 K for $x = 0$ and 12 K for $x = 0.2$, 0.4, and 0.9. Panels (e)–(h) show zoomed-in regions in which the main magnetic peaks are visible for the $x = 0$, 0.2, and 0.4 samples. The $x = 0.9$ sample does not exhibit long-range magnetic order.

function of Lu content. Nonetheless, it lies somewhere between $x = 0.5$ and $x = 0.6$.

The temperature dependence of magnetic structures of $x = 0.1$ and 0.2 correlates well with the hump observed in their 1 T magnetization data. This correlation is evident in the nonmonotonic evolution of the magnetic structure and the expected hump-related spin reorientation in both the kagome and triangular layers. The magnitude and direction of the magnetic moment of the Co5-Co6 pairs change nonmonotonically as a function of temperature. The magnetic structure for $x = 0.1$ at 12 and 20 K and for $x = 0.2$ at 12 K (well below the magnetization hump) shows that the Co3-Co4 and Co7-Co8 ribbons' magnetic moments are coupled ferromagnetically and antiferromagnetically to their neighbors along the stripe direction in an "up-up-down-down" pattern. At higher temperatures up to $\approx 60$ K (near the magnetization hump), the magnetic moments rotate to form a zigzag pattern. Above $\approx 60$ K (well above the magnetization hump), the magnetic

moments continue their rotation to align along the $[1\bar{1}0]$ direction.

Figure 14 presents the Co magnetic moments at 12 K refined as a function of Lu content. For $x = 0.0$, magnetic moment magnitudes of 3.19(6), 2.71(6), 2.69(8), and 2.60(9) $\mu_B$ were obtained for the Co1-Co2, Co3-Co4, Co5-Co6, and Co7-Co8 pairs, respectively. The smaller than expected magnetic moments (3 and 4 $\mu_B$ for high-spin Co$^{2+}$ and Co$^{3+}$ states, respectively) may be explained by crystal field quenching effects and the persistence of significant and continuously enhanced short-range magnetic correlations with increasing Lu. Similarly, lower than expected magnetic moment magnitudes were observed by Khalyavin *et al.* [24] at 5 K and explained by the coexistence of diffuse scattering arising from fractional disorder of the magnetic moments together with the long-range ordered magnetic Co sublattice. The magnetic moments of Co1-Co2, Co3-Co4, and Co7-Co8 decrease linearly as a function of increased Lu content. Extrapolating the linear fits
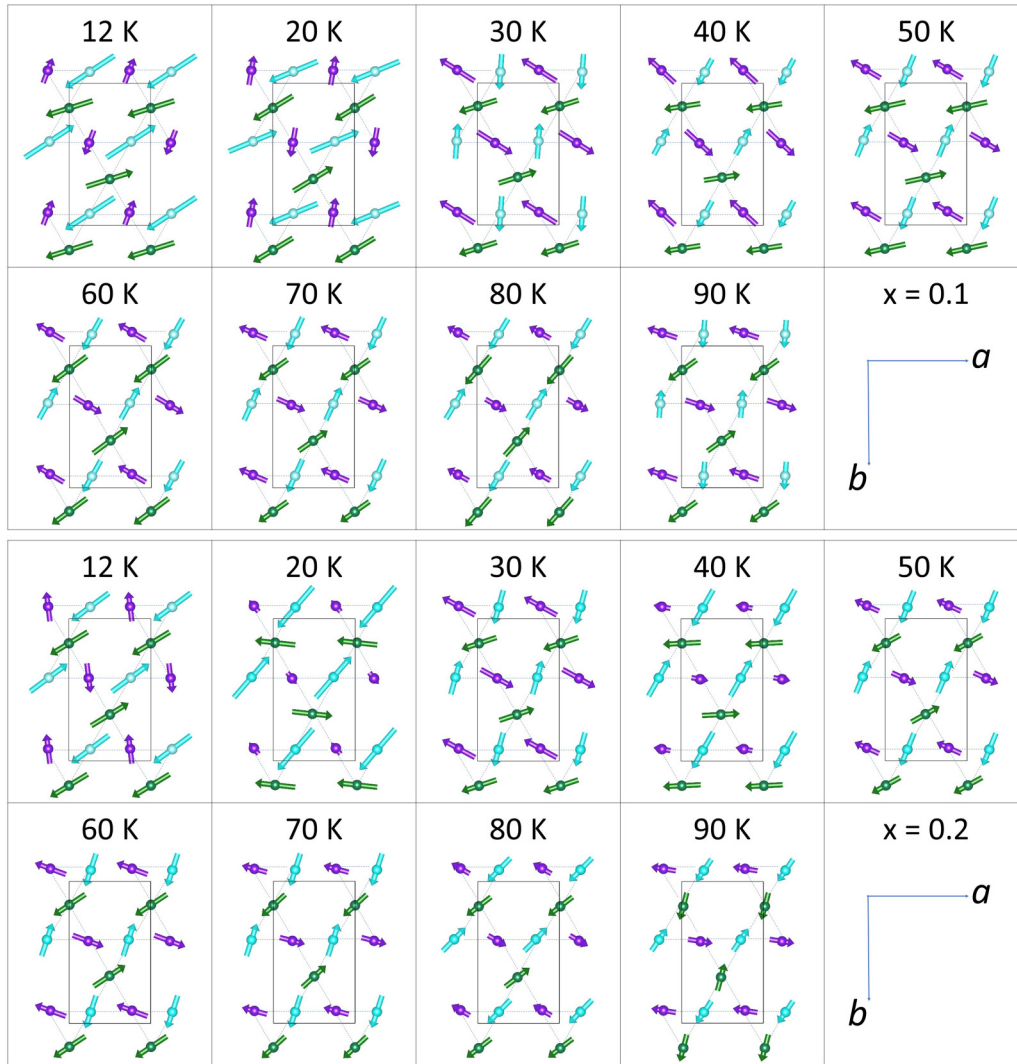
FIG. 13. Effects of the temperature on the magnetic structure of the kagome layer for the $x = 0.1$ and 0.2 samples. In these representations, atom pairs that align antiferromagnetically share the same color: Co3-Co4 pairs are green, Co5-Co6 pairs are purple, and Co7-Co8 pairs are cyan. The arrows indicate the relative magnetic moments, all of which lie in the $ab$ plane based on the magnetic $P12'_1 1$ symmetry. The neutron diffraction data were collected on warming after fast cooling ($\approx 3.5$ K/min) down to 12 K.

shows that vanishing magnetic moments would be achieved for $x$ between 0.8 and 0.9, consistent with the weak and broad neutron diffraction magnetic peaks disappearing at the same $x$ values as shown in Fig. 3(b). The Co5-Co6 magnetic moment behavior, however, remains roughly constant for the substituted samples.

Figure 15 shows the Co magnetic moments as a function of temperature for $x = 0.1$ and 0.2. The overall features of the magnetic moment behaviors are similar for both samples, despite the larger scatter observed for $x = 0.2$ due to weaker long-range magnetic moment magnitudes.

## IV. CONCLUSIONS

This study establishes the impact of Lu substitution on the magnetic and structural properties of the geometrically frustrated YBaCo$_4$O$_7$ antiferromagnet. The full phase diagram of Y$_{1-x}$Lu$_x$BaCo$_4$O$_7$ is mapped out through temperature-dependent high-resolution neutron powder diffraction and magnetometry. Lu substitution reduces the orthorhombic $Pbn2_1$ phase transition temperature from 310 K ($x = 0.0$) to 110 K ($x = 1.0$). On the Lu side of the phase diagram (with $x \geqslant 0.7$), a metastable monoclinic $Cc$ phase coexists with the orthorhombic $Pbn2_1$ phase. The phase fraction of the monoclinic $Cc$ phase decreases with increasing Lu content, correlating with the weakening peak in the magnetization of these samples. The unit cell parameters $a$ and $b$, and the volume decrease linearly with increasing Lu content due to the smaller ionic radius of Lu compared to Y while the $c$ axis is minimally affected.

Long-range AFM order observed below 110 K in YBaCo$_4$O$_7$ diminishes rapidly with increasing Lu content, leaving only short-range correlations for $x > 0.5$. Magnetic structures for all samples with $x \leqslant 0.5$ were determined, and changes in the magnetic moments were correlated with the cusp/hump feature observed in the magnetization data of the Y-rich compositions. The refinements demonstrate the antiferromagnetic alignment of specific Co atom pairs in the
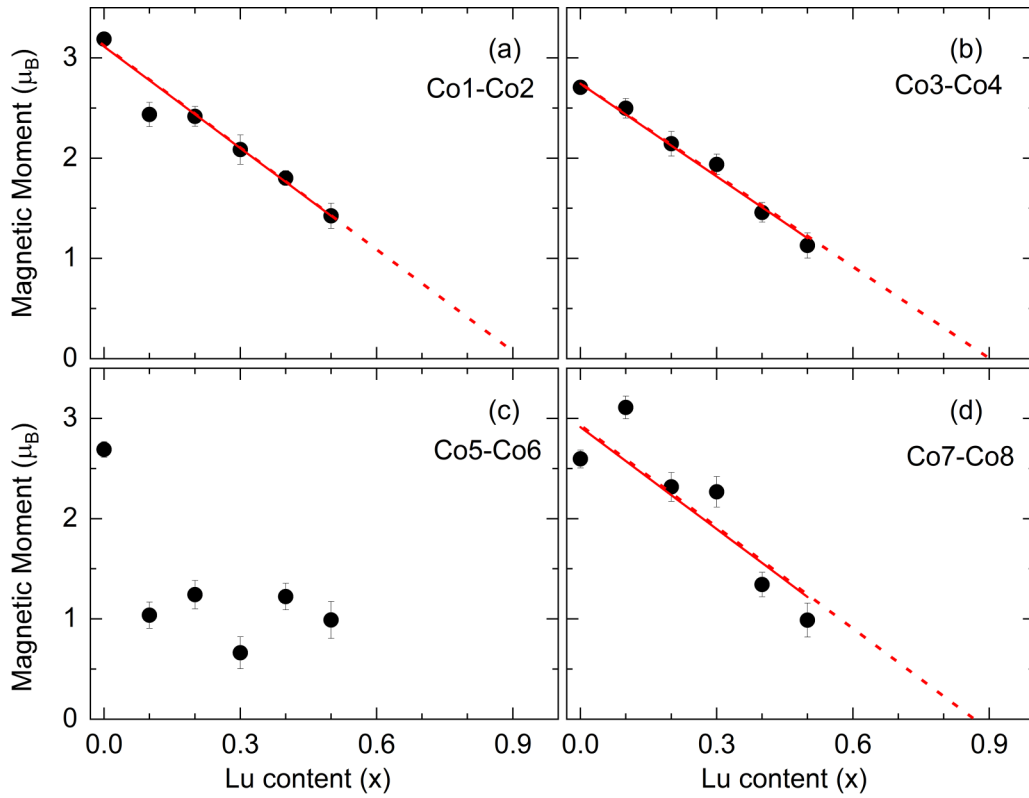
FIG. 14. Magnetic moments of Co1-Co2, Co3-Co4, Co5-Co6, and Co7-Co8 as a function of Lu content. The red solid lines represent linear fits to the data, providing a visual guide. The red dotted lines show extrapolations of the linear fits. Neutron diffraction data were collected at 5 K for the $x = 0.0$ sample and at 12 K for all the Lu-substituted samples after fast cooling ($\approx$3.5 K/min).
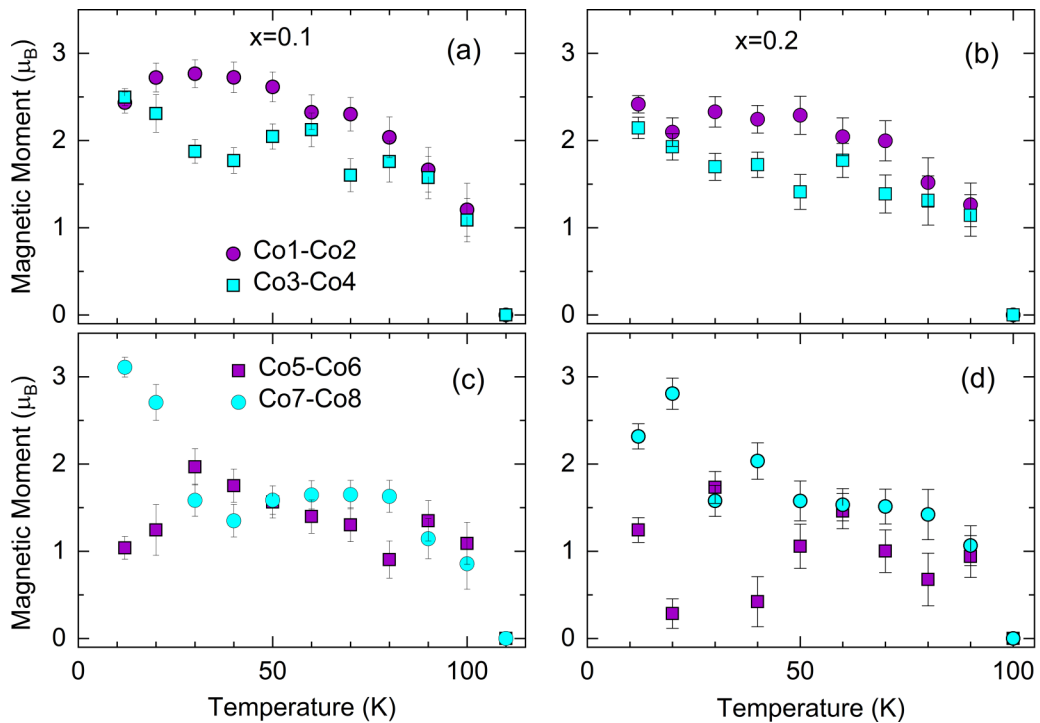


FIG. 15. Magnetic moments of Co1-Co2 and Co3-Co4 (a),(b), and Co5-Co6 and Co7-Co8 (c),(d) as a function of temperature for $x = 0.1$ (left panels) and $x = 0.2$ (right panels). The neutron diffraction data were collected on warming after fast cooling ($\approx$3.5 K/min) down to 12 K.

*ab* plane in both the kagome and triangular layers. Some moments in the kagome layers align nearly parallel giving the appearance of "ribbons" along one of the *ab* plane diagonals.

## ACKNOWLEDGMENTS

[1] S. Nakatsuji, Y. Nambu, H. Tonomura, O. Sakai, S. Jonas, C. Broholm, H. Tsunetsugu, Y. Qiu, and Y. Maeno, Spin disorder on a triangular lattice, Science **309**, 1697 (2005).

[2] M. F. Collins and O. A. Petrenko, Review/Synthèse: Triangular antiferromagnets, Can. J. Phys. **75**, 605 (1997).

[3] T. Katsufuji, S. Mori, M. Masaki, Y. Moritomo, N. Yamamoto, and H. Takagi, Dielectric and magnetic anomalies and spin frustration in hexagonal $R$MnO$_3$ ($R$ = Y, Yb, and Lu), Phys. Rev. B **64**, 104419 (2001).

[4] J. N. Reimers, A. J. Berlinsky, and A.-C. Shi, Mean-field approach to magnetic ordering in highly frustrated pyrochlores, Phys. Rev. B **43**, 865 (1991).

[5] X.-Y. Wang, L. Wang, Z.-M. Wang, and S. Gao, Solvent-tuned azido-bridged Co$^{2+}$ layers: Square, honeycomb, and kagomé, J. Am. Chem. Soc. **128**, 674 (2006).

[6] R. Moessner and S. L. Sondhi, Ising models of quantum frustration, Phys. Rev. B **63**, 224401 (2001).

[7] E. Mengotti, L. J. Heyderman, A. F. Rodríguez, F. Nolting, R. V. Hügli, and H.-B. Braun, Real-space observation of emergent magnetic monopoles and associated Dirac strings in artificial kagome spin ice, Nat. Phys. **7**, 68 (2011).

[8] R. Moessner and J. T. Chalker, Properties of a classical spin liquid: The Heisenberg pyrochlore antiferromagnet, Phys. Rev. Lett. **80**, 2929 (1998).

[9] S.-H. Lee, C. Broholm, W. Ratcliff, G. Gasparovic, Q. Huang, T. H. Kim, and S.-W. Cheong, Emergent excitations in a geometrically frustrated magnet, Nature (London) **418**, 856 (2002).

[10] S. T. Bramwell and M. J. P. Gingras, Spin ice state in frustrated magnetic pyrochlore materials, Science **294**, 1495 (2001).

[11] M. J. Harris, S. T. Bramwell, D. F. McMorrow, T. Zeiske, and K. W. Godfrey, Geometrical frustration in the ferromagnetic pyrochlore Ho$_2$Ti$_2$O$_7$, Phys. Rev. Lett. **79**, 2554 (1997).

[12] S. Avci, O. Chmaissem, H. Zheng, A. Huq, D. D. Khalyavin, P. W. Stephens, M. R. Suchomel, P. Manuel, and J. F. Mitchell, Kinetic control of structural and magnetic states in LuBaCo$_4$O$_7$, Phys. Rev. B **85**, 094414 (2012).

[13] L. C. Chapon, P. G. Radaelli, H. Zheng, and J. F. Mitchell, Competing magnetic interactions in the extended kagomé system YBaCo$_4$O$_7$, Phys. Rev. B **74**, 172401 (2006).

[14] M. Soda, K. Morita, G. Ehlers, F. Ye, T. Tohyama, H. Yoshizawa, T. Masuda, and H. Kawano-Furukawa, Magnetic diffuse scattering of YBaCo$_4$O$_7$ and LuBaCo$_4$O$_7$ on kagome and triangular lattices, J. Phys. Soc. Jpn. **90**, 074704 (2021).

[15] T. Sarkar, M. M. Seikh, V. Pralong, V. Caignaert, and B. Raveau, Magnetism of the "114" orthorhombic charge ordered CaBaCo$_4$O$_7$ doped with Zn or Ga: A spectacular valency effect, J. Mater. Chem. **22**, 18043 (2012).

[16] A. Huq, J. F. Mitchell, H. Zheng, L. C. Chapon, P. G. Radaelli, K. S. Knight, and P. W. Stephens, Structural and magnetic properties of the kagomé antiferromagnet YbBaCo$_4$O$_7$, J. Solid State Chem. **179**, 1136 (2006).

[17] T. Sarkar, V. Caignaert, V. Pralong, and B. Raveau, Hysteretic "magnetic-transport-structural" transition in "114" cobaltites: Size mismatch effect, Chem. Mater. **22**, 6467 (2010).

[18] N. Nakayama, T. Mizota, Y. Ueda, A. N. Sokolov, and A. N. Vasiliev, Structural and magnetic phase transitions in mixed-valence cobalt oxides $RE$BaCo$_4$O$_7$ ($RE$ = Lu, Yb, Tm), J. Magn. Magn. Mater. **300**, 98 (2006).

[19] A. Maignan, V. Caignaert, V. Pralong, D. Pelloquin, and S. Hébert, Impact of metal substitutions for cobalt in YBaCo$_4$O$_7$, J. Solid State Chem. **181**, 1220 (2008).

[20] M. Y. Ruan, Z. W. Ouyang, Y. M. Guo, Y. C. Sun, J. J. Cheng, Z. C. Xia, and G. H. Rao, Spin-glass-like freezing in geometrically frustrated compound InBaCo$_4$O$_7$, Solid State Sci. **45**, 1 (2015).

[21] V. Caignaert, V. Pralong, A. Maignan, and B. Raveau, Orthorhombic kagome cobaltite CaBaCo$_4$O$_7$: A new ferrimagnet with a $T_C$ of 70 K, Solid State Commun. **149**, 453 (2009).

[22] Z. Qu, L. Ling, L. Zhang, L. Pi, and Y. Zhang, Magnetic properties of the ferrimagnetic cobaltite CaBaCo$_4$O$_7$, Solid State Commun. **151**, 917 (2011).

[23] P. Manuel, L. C. Chapon, P. G. Radaelli, H. Zheng, and J. F. Mitchell, Magnetic correlations in the extended kagome YBA Co$_4$O$_7$ PROBED by single-crystal neutron scattering, Phys. Rev. Lett. **103**, 037202 (2009).

[24] D. D. Khalyavin, P. Manuel, B. Ouladdiaf, A. Huq, P. W. Stephens, H. Zheng, J. F. Mitchell, and L. C. Chapon, Spin-ordering and magnetoelastic coupling in the extended kagome system YBaCo$_4$O$_7$, Phys. Rev. B **83**, 094412 (2011); **83**, 219902(E) (2011); **85**, 059903(E) (2012).

[25] M. J. R. Hoch, P. L. Kuhns, S. Yuan, T. Besara, J. B. Whalen, T. Siegrist, A. P. Reyes, J. S. Brooks, H. Zheng, and J. F. Mitchell, Evidence for an internal-field-induced spin-flop configuration in the extended kagome YBaCo$_4$O$_7$, Phys. Rev. B **87**, 064419 (2013).

[26] A. Huq, M. Kirkham, P. F. Peterson, J. P. Hodges, P. S. Whitfield, K. Page, T. Hugle, E. B. Iverson, A. Parizzia, and G. Rennichb, POWGEN: Rebuild of a third-generation powder diffractometer at the spallation neutron source, J. Appl. Crystallogr. **52**, 1189 (2019).

[27] H. M. Rietveld, A profile refinement method for nuclear and magnetic structures, J. Appl. Crystallogr. **2**, 65 (1969).

[28] B. H. Toby and R. B. Von Dreele, GSAS-II: The genesis of a modern open-source all purpose crystallography software package, J. Appl. Crystallogr. **46**, 544 (2013).

[29] K. Momma and F. Izumi, VESTA 3 for three-dimensional visualization of crystal, volumetric and morphology data, J. Appl. Crystallogr. **44**, 1272 (2011).

[30] See Supplemental Material at http://link.aps.org/supplemental/10.1103/PhysRevB.110.014438 for additional information on structures, magnetic properties and neutron powder diffraction.

[31] S. Lee, W. Lee, K. J. Lee, B. J. Kim, B. J. Suh, H. Zheng, J. F. Mitchell, and K. Y. Choi, Muon spin relaxation study of spin dynamics in the extended kagome systems YBaCo$_4$O$_{7+\delta}$($\delta = 0, 0.1$), Phys. Rev. B **97**, 104409 (2018).

[32] L. Vegard, Die konstitution der mischkristalle und die raumfüllung der atome, Z. Phys. **5**, 17 (1921).

[33] R. D. Shannon, Revised effective ionic radii and systematic studies of interatomic distances in halides and chalcogenides, Acta Crystallogr., Sect. A **32**, 751 (1976).